46th AIAA/ASME/SAE/ASEE Joint Propulsion Conference & Exhibit
25 - 28 July 2010, Nashville, TN

AIAA 2010-6652

On the Bidirectional Vortex with Arbitrary Endwall Velocity

Georges Akiki* and Joseph Majdalani†
University of Tennessee Space Institute, Tullahoma, TN 37388

In this study, an exact solution is derived for the bidirectional vortex field in a right-cylindrical chamber. The cyclonic motion is assumed to be axisymmetric, steady, inviscid and incompressible, with no accounting for reactions or heat transfer. Our approach is based on the Bragg-Hawthorne equation (BHE), which can be solved in our situation under conditions leading to linearity. Using separation of variables, we are able to identify a set of eigensolutions that may be associated with this problem. The linearity of the resulting BHE enables us to superimpose these eigensolutions while making use of orthogonality to the extent of accommodating different injection configurations that may be imposed at the open boundaries. Finally, the theoretical results are compared to other analytical solutions and experimental results. Our idealization is applicable to incompressible representations of cyclone-driven industrial flow separators, vacuum chambers, furnaces, plasma generators, and liquid rocket engines.

Nomenclature

A_i = inlet area
a = chamber radius
B = tangential angular momentum, ru_θ
b = chamber outlet radius
H = stagnation pressure head
L = chamber length
l = chamber aspect ratio, L/a
Q_i = inlet volumetric flow rate
r, θ, z = radial, tangential, and axial coordinates
U = mean tangential (inflow) velocity
$U_0(r)$ = arbitrary axial velocity at the headwall
$U_L(r)$ = arbitrary axial velocity at the endwall
u_r = dimensional radial velocity
u_θ = dimensional tangential velocity
u_z = dimensional axial velocity

Symbols

κ = tangential inflow parameter, $(2\pi\sigma l)^{-1}$
λ_n = nth zero of J_1, the Bessel function of the first kind
σ = swirl number
υ = separation constant
ψ = stream function
$\bar{}$ = overbars denote a nondimensional variable

*Graduate Research Assistant, Mechanical, Aerospace and Biomedical Engineering Department. Member AIAA.
†H. H. Arnold Chair of Excellence in Advanced Propulsion, Mechanical, Aerospace and Biomedical Engineering Department. Senior Member AIAA. Fellow ASME.

I. Introduction

BESIDES their emergence in naturally occurring phenomena, cyclonic motions arise in a variety of industrial and propulsion related applications. These swirl-induced patterns are connected to meteorological events such as tornadoes, hurricanes and typhoons, as well as astronomical activities such as cosmic spirals and galactic pinwheels. The bidirectional type of motion is also employed in industrial processes involving cyclonic separators, combustors, and furnaces. Our main interest here is tied to the cyclonic motion that is engendered in the vortex-fired engine class of propulsion devices. This class encompasses several innovative internal combustion devices and thrust chambers such as the Vortex Hybrid Engine introduced by Gloyer, Knuth and Goodman,[1] the Vortex Injection Hybrid Rocket Engine conceived by Knuth *et al*.,[2] the Vortex Combustion Cold-Wall Chamber developed by Chiaverini *et al.*,[3] and the Reverse Vortex Combustor invented by Matveev *et al*.[4]

Given the shortage of purely analytical models of axisymmetric cyclonic flows, an Eulerian-based solution was developed by Vyas, Majdalani and Chiaverini[5-7] using a right-cylindrical Vortex Combustion Cold-Wall Chamber model. Their effort set the pace for a laminar boundary layer treatment of the viscous core. Shortly thereafter, the extension to the hybrid vortex configuration was conceived and carried out by Majdalani and Vyas,[8] and later generalized by Majdalani[9] for the case involving sidewall mass addition. As for the sidewall boundary layers, they were resolved under laminar conditions by Vyas and Majdalani[10] and then, for the axial and radial orientation, by Batterson and Majdalani.[11,12] The latest investigation by Majdalani and Chiaverini[13] formalized the analysis of the tangential boundary layers in a bidirectional vortex, specifically those forming at the core and the sidewall of a swirl-driven cyclonic chamber. A piecewise representation of the problem leading to a Rankine-like vortex was also developed by Maicke and Majdalani.[14] Solutions for other cyclonic flows were obtained by Zhao and Abrahamson[15] who investigated gas cyclones with flow patterns resembling those entailed in the bidirectional vortex engine.

In this paper, we consider the Bragg-Hawthorne equation with assumptions leading to linear source terms. Subsequent analysis based on separation of variables gives rise to three possible types of solutions. After showing that one type is a special case, the remaining two are explored and shown to provide eigensolutions that can be combined linearly. Their superposition leads to a Fourier-like series that can be used in conjunction with the

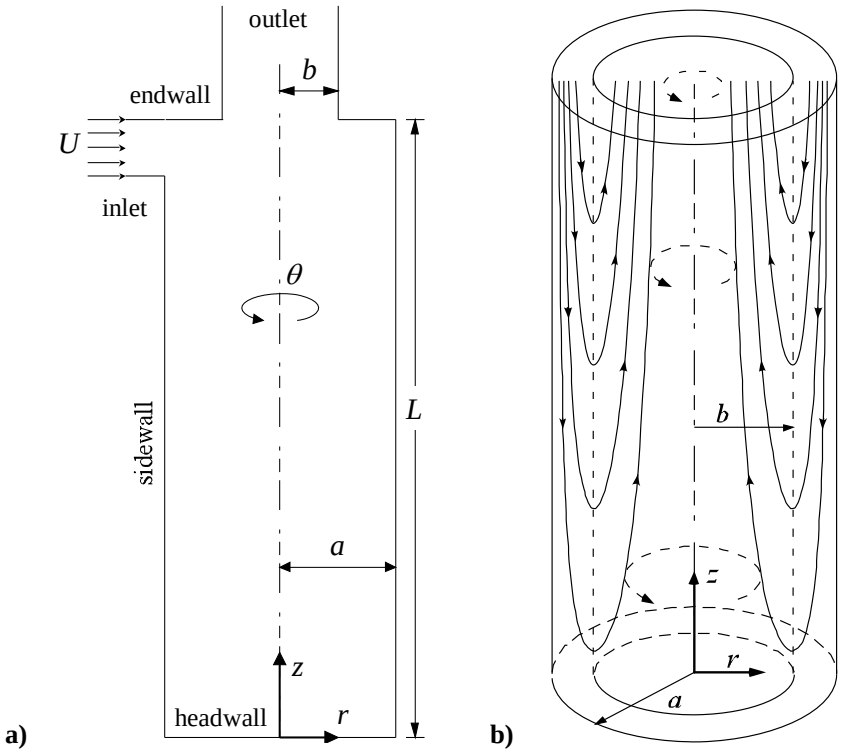

Figure 1. Schematic diagram of the cylindrical bidirectional vortex chamber showing a) geometric and b) flowfield characteristics.

orthogonality concept to produce exact inviscid solutions that can accommodate a fixed flow profile at the endwalls. The superposition of the solutions is plausible in our case due to the linearity of the equation being solved. The mathematical framework thus developed enables us to model the flow with realistic inlet conditions.

II. Formulation

A. Mathematical Model

Since we are dealing with the axisymmetric bidirectional vortex in a chamber with circular cross-section, cylindrical coordinates are used. Our intent is to solve the applicable equations of motion with the aim of constructing analytical solutions for a user-prescribed set of boundary conditions. Our model is sketched in Fig. 1 where a schematic diagram of the physical problem is provided along with its flowfield characteristics. Note that an inlet section is located near $z = L$ to permit the injection of fluid with arbitrary velocity.

As usual, the incompressible momentum equations for a steady axisymmetric inviscid flow can be written as

$$u_z \frac{\partial u_z}{\partial z} + u_r \frac{\partial u_z}{\partial r} = -\frac{1}{\rho}\frac{\partial p}{\partial z} \tag{1}$$

$$u_z \frac{\partial u_r}{\partial z} + u_r \frac{\partial u_r}{\partial r} - \frac{u_\theta^2}{r} = -\frac{1}{\rho}\frac{\partial p}{\partial r} \tag{2}$$

$$u_z \frac{\partial u_\theta}{\partial z} + u_r \frac{\partial u_\theta}{\partial r} + \frac{u_\theta u_r}{r} = 0 \tag{3}$$

with the attending continuity equation

$$\frac{\partial u_z}{\partial z} + \frac{1}{r}\frac{\partial (r u_r)}{\partial r} = 0 \tag{4}$$

Using the streamfunction ψ, such that $u_z = r^{-1}\partial\psi/\partial r$ and $u_r = -r^{-1}\partial\psi/\partial z$, the above set may be transformed into a single expression known as the Bragg-Hawthorne equation (BHE),

$$\frac{\partial^2 \psi}{\partial z^2} + \frac{\partial^2 \psi}{\partial r^2} - \frac{1}{r}\frac{\partial \psi}{\partial r} = r^2 \frac{\mathrm{d}H}{\mathrm{d}\psi} - B\frac{\mathrm{d}B}{\mathrm{d}\psi} \tag{5}$$

Here $H = p/\rho + \frac{1}{2}u^2$ and $B = r u_\theta$ represent the total pressure head and tangential angular momentum, respectively.

In the absence of friction and heat addition, our model may be taken to be isentropic. This restricts the total pressure head to remain constant along streamlines where $\mathrm{d}H/\mathrm{d}\psi = 0$.

To further simplify the problem, we follow the approach used by Majdalani[16] and take the second term on the right-hand-side (RHS) of Eq. (5) to be a linear function of ψ. We therefore put

$$B\frac{\mathrm{d}B}{\mathrm{d}\psi} = C^2\psi \tag{6}$$

and collect

$$\frac{\partial^2 \psi}{\partial z^2} + \frac{\partial^2 \psi}{\partial r^2} - \frac{1}{r}\frac{\partial \psi}{\partial r} + C^2\psi = 0 \tag{7}$$

Equation (7) can be solved using separation of variables assuming a rigid sidewall with

$$u_r(0, z) = 0 \tag{8}$$

$$u_r(a, z) = 0 \tag{9}$$

We can also account for arbitrary endwall injection by setting

$$u_z(r, 0) = U_0(r) \qquad \text{and} \qquad u_z(r, L) = U_L(r) \tag{10}$$

where $U_0(r)$ and $U_L(r)$ can be user-specified to capture realistic flow patterns that observe the mass conservation principle. Substituting $\psi(z, r) = Z(z)R(r)$ into Eq. (7) leads to

$$-\frac{1}{Z(z)}\frac{\mathrm{d}^2 Z(z)}{\mathrm{d}z^2} = \frac{1}{R(r)}\frac{\mathrm{d}^2 R(r)}{\mathrm{d}r^2} - \frac{1}{rR(r)}\frac{\mathrm{d}R(r)}{\mathrm{d}r} + C^2 = \begin{cases} 0 \\ \pm\upsilon^2 \end{cases} \tag{11}$$

Clearly, three cases may be identified and promptly classified as

Type 0 with $\mathrm{RHS} = 0$:

$$\psi(r, z) = r\left(C_1 z + C_2\right)\left[C_3 J_1(Cr) + C_4 Y_1(Cr)\right] \tag{12}$$

Type I with $\text{RHS} = +\upsilon^2$:

$$\psi(r,z) = r\left[C_1 \sin(\upsilon\, z) + C_2 \cos(\upsilon\, z)\right]\left[C_3 J_1\left(r\sqrt{C^2-\upsilon^2}\right) + C_4 Y_1\left(r\sqrt{C^2-\upsilon^2}\right)\right] \tag{13}$$

Type II with $\text{RHS} = -\upsilon^2$:

$$\psi(r,z) = r\left[C_1 \sinh(\upsilon\, z) + C_2 \cosh(\upsilon\, z)\right]\left[C_3 J_1\left(r\sqrt{C^2+\upsilon^2}\right) + C_4 Y_1\left(r\sqrt{C^2+\upsilon^2}\right)\right] \tag{14}$$

When imposing the centerline condition defined by Eq. (8), we retrieve $C_4 = 0$ and so prevent $Y_1(Cr)$, $Y_1[r(C^2-\upsilon^2)^{\frac{1}{2}}]$ and $Y_1[r(C^2+\upsilon^2)^{\frac{1}{2}}]$ from approaching infinity as $r \to 0$. The solution set reduces to

$$\psi(r,z) = \begin{cases} r\left(K_1 z + K_2\right) J_1(Cr) & \text{(type 0)} \\ r\left[K_1 \sin(\upsilon\, z) + K_2 \cos(\upsilon\, z)\right] J_1\left(r\sqrt{C^2-\upsilon^2}\right) & \text{(type I)} \\ r\left[K_1 \sinh(\upsilon\, z) + K_2 \cosh(\upsilon\, z)\right] J_1\left(r\sqrt{C^2+\upsilon^2}\right) & \text{(type II)} \end{cases} \tag{15}$$

where $K_1 = C_1 C_3$ and $K_2 = C_2 C_3$. Subsequently, the application of Eq. (9), the rigid wall condition on the radial velocity, leads to two sets of eigenvalues:

$$J_1\left(a\sqrt{C^2-\upsilon^2}\right) = 0 \qquad \text{or} \qquad \upsilon = \upsilon_n = \sqrt{C^2 - \lambda_n^2 / a^2} \qquad \text{(type I)} \tag{16}$$

$$J_1\left(a\sqrt{C^2+\upsilon^2}\right) = 0 \qquad \text{or} \qquad \upsilon = \upsilon_n^* = \sqrt{\lambda_n^2 / a^2 - C^2} \qquad \text{(type II)} \tag{17}$$

where $\lambda_n = (3.83171, 7.01559, 10.1735, 13.3237, ...)$ designates the set of roots connected with the Bessel function of the first kind. In what follows, the multivalued nature of λ_n warrants the use of υ_n and υ_n^*. In the type 0 formulation, the streamfunction remains independent of υ, a situation that leads to a limited solution, especially that C must remain single-valued, as prescribed by Eq. (6). A more general framework may be established by summing over all λ_n and putting, for the type I and type II solutions

$$\psi(r,z) = \begin{cases} \displaystyle\sum_{n=0}^{\infty} r\left[K_{1n} \sin(\upsilon_n z) + K_{2n} \cos(\upsilon_n z)\right] J_1(\lambda_n r / a) & \text{(type I)} \\ \displaystyle\sum_{n=0}^{\infty} r\left[K_{1n} \sinh(\upsilon_n^* z) + K_{2n} \cosh(\upsilon_n^* z)\right] J_1(\lambda_n r / a) & \text{(type II)} \end{cases} \tag{18}$$

The corresponding axial velocity may be expressed as

$$u_z = \begin{cases} \displaystyle\sum_{n=0}^{\infty}\left[K_{1n} \sin(\upsilon_n z) + K_{2n} \cos(\upsilon_n z)\right] \frac{\lambda_n}{a} J_0\left(\frac{\lambda_n}{a} r\right) & \text{(type I)} \\ \displaystyle\sum_{n=0}^{\infty}\left[K_{1n} \sinh(\upsilon_n^* z) + K_{2n} \cosh(\upsilon_n^* z)\right] \frac{\lambda_n}{a} J_0\left(\frac{\lambda_n}{a} r\right) & \text{(type II)} \end{cases} \tag{19}$$

At this junction, one may impose an arbitrary velocity profile at the endwalls by specifying $u_z(r,0) = U_0(r)$ and $u_z(r,L) = U_L(r)$ as per Eq. (10). Using the orthogonality function, we recall that

$$\int_0^a r J_0(mr) J_0(nr)\, \mathrm{d}r = \begin{cases} 0; & m \neq n \\ \frac{1}{2} a^2 J_0^2(ma); & m = n \end{cases} \tag{20}$$

Then through backward substitutions, the two constants K_{1n} and K_{2n} may be extracted into

$$K_{1n} = \begin{cases} \dfrac{I_L - \cos(\upsilon_n L) I_0}{\lambda_n a J_0^2(\lambda_n) \sin(\upsilon_n L)} \\ \dfrac{I_L - \cosh(\upsilon_n^* L) I_0}{\lambda_n a J_0^2(\lambda_n) \sinh(\upsilon_n^* L)} \end{cases} \quad \text{and} \quad K_{2n} = \begin{cases} \dfrac{I_0}{\lambda_n a J_0^2(\lambda_n)} \\ \dfrac{I_0}{\lambda_n a J_0^2(\lambda_n)} \end{cases} \tag{21}$$

The source terms in Eq. (21) may be determined from

$$I_0 \equiv 2\int_0^a U_0(r) r J_0(\lambda_n r / a)\, \mathrm{d}r \quad \text{and} \quad I_L \equiv 2\int_0^a U_L(r) r J_0(\lambda_n r / a)\, \mathrm{d}r \tag{22}$$

Inserting these relations back into Eq. (18) and differentiating, general expressions for the axial and radial velocities may be consecutively returned,

$$u_z = \begin{cases} \displaystyle\sum_{n=0}^{\infty}\left[\frac{I_L-\cos(\upsilon_n L)I_0}{\lambda_n a J_0^2(\lambda_n)}\frac{\sin(\upsilon_n z)}{\sin(\upsilon_n L)}+\frac{I_0}{\lambda_n a J_0^2(\lambda_n)}\cos(\upsilon_n z)\right]J_0\left(\frac{\lambda_n}{a}r\right) & \text{(type I)} \\ \displaystyle\sum_{n=0}^{\infty}\left[\frac{I_L-\cosh(\upsilon_n^* L)I_0}{\lambda_n a J_0^2(\lambda_n)}\frac{\sinh(\upsilon_n^* z)}{\sinh(\upsilon_n^* L)}+\frac{I_0}{\lambda_n a J_0^2(\lambda_n)}\cosh(\upsilon_n^* z)\right]J_0\left(\frac{\lambda_n}{a}r\right) & \text{(type II)} \end{cases} \tag{23}$$

and

$$u_r = \begin{cases} \displaystyle-\sum_{n=0}^{\infty}\left[\frac{I_L-\cos(\upsilon_n L)I_0}{\lambda_n a J_0^2(\lambda_n)}\frac{\upsilon_n}{\sin(\upsilon_n L)}\cos(\upsilon_n z)-\frac{I_0}{\lambda_n a J_0^2(\lambda_n)}\upsilon_n\sin(\upsilon_n z)\right]J_1\left(\frac{\lambda_n}{a}r\right) & \text{(type I)} \\ \displaystyle-\sum_{n=0}^{\infty}\left[\frac{I_L-\cosh(\upsilon_n^* L)I_0}{\lambda_n a J_0^2(\lambda_n)}\frac{\upsilon_n^*}{\sinh(\upsilon_n^* L)}\cosh(\upsilon_n^* z)+\frac{I_0}{\lambda_n a J_0^2(\lambda_n)}\upsilon_n^*\sinh(\upsilon_n^* z)\right]J_1\left(\frac{\lambda_n}{a}r\right) & \text{(type II)} \end{cases} \tag{24}$$

As for the tangential velocity u_θ, we can start with Eq. (6) and integrate $\int B\mathrm{d}B = \int C_n^2\psi\mathrm{d}\psi$ to obtain

$$B^2 = C^2\psi^2 + B_1 \quad \text{or} \quad u_\theta = r^{-1}\sqrt{C^2\psi^2+B_1} \tag{25}$$

Then by inserting ψ into Eq. (25), an expanded form of u_θ is arrived at, specifically

$$ru_\theta = \begin{cases} \left\{C^2\left[\displaystyle\sum_{n=0}^{\infty} r\left(\frac{I_L-\cos(\upsilon_n L)I_0}{\lambda_n a J_0^2(\lambda_n)}\frac{\sin(\upsilon_n z)}{\sin(\upsilon_n L)}+\frac{I_0}{\lambda_n a J_0^2(\lambda_n)}\cos(\upsilon_n z)\right)J_1\left(\frac{\lambda_n}{a}r\right)\right]^2+B_1\right\}^{\frac{1}{2}} & \text{(type I)} \\ \left\{C^2\left(\displaystyle\sum_{n=0}^{\infty} r\left[\frac{I_L-\cosh(\upsilon_n^* L)I_0}{\lambda_n a J_0^2(\lambda_n)}\frac{\sinh(\upsilon_n^* z)}{\sinh(\upsilon_n^* L)}+\frac{I_0}{\lambda_n a J_0^2(\lambda_n)}\cosh(\upsilon_n^* z)\right]J_1\left(\frac{\lambda_n}{a}r\right)\right)^2+B_1\right\}^{\frac{1}{2}} & \text{(type II)} \end{cases} \tag{26}$$

Note that C appears outside the summation due to nonlinearity in the relation between u_θ and ψ. It therefore retains a unique value irrespective of the eigensolutions that are being superimposed in Eq. (26).

B. Consolidated Solution

At first glance, the two types of solutions captured in Eqs. (23), (24), and (26) appear dissimilar. Upon further scrutiny, however, we find that one may be restored from the other for $\upsilon_n^2 = i^2(\upsilon_n^*)^2$ or $\upsilon_n = \pm i(\upsilon_n^*)$. This is due to the trigonometric identities

$$\begin{cases} \cosh x = \cos(ix) \\ \sinh x = -i\sin(ix) \end{cases} \quad \text{or} \quad \begin{cases} \cosh\upsilon_n^* = \cos(i\upsilon_n^*) = \cos\upsilon_n \\ \sinh\upsilon_n^* = -i\sin(i\upsilon_n^*) = -i\sin(\pm ii\upsilon_n) = \pm i\sin(\upsilon_n) \end{cases} \tag{27}$$

which are needed to change type II into type I, or conversely, through

$$\begin{cases} \cos x = \cosh(ix) \\ \sin x = -i\sinh(ix) \end{cases} \quad \text{or} \quad \begin{cases} \cos\upsilon_n = \cosh(i\upsilon_n) = \cosh(\upsilon_n^*) \\ \sin\upsilon_n = -i\sinh(i\upsilon_n) = -i\sinh(\pm ii\upsilon_n^*) = \pm i\sinh(\upsilon_n^*) \end{cases} \tag{28}$$

These identities enable us to confirm by inspection the equality of the two types of solutions obtained for u_θ and u_z. In the interest of clarity, we show how this can be performed for u_r. By substituting $\upsilon_n^* = \pm i\upsilon_n$ into the second member of Eq. (24) and using both $\cosh(i\upsilon_n z) = \cos(\upsilon_n z)$ and $\sinh(i\upsilon_n z) = i\sin(\upsilon_n z)$, we have

$$\begin{aligned} u_r &= -\sum_{n=0}^{\infty}\left[\frac{I_L-\cosh(\pm i\upsilon_n L)I_0}{\lambda_n a J_0^2(\lambda_n)}\frac{(\pm i\upsilon_n)}{\sinh(\pm i\upsilon_n L)}\cosh(\pm i\upsilon_n z)+\frac{I_0}{\lambda_n a J_0^2(\lambda_n)}(\pm i\upsilon_n)\sinh(\pm i\upsilon_n z)\right]J_1\left(\frac{\lambda_n}{a}r\right) \\ &= -\sum_{n=0}^{\infty}\left[\frac{I_L-\cosh(i\upsilon_n L)I_0}{\lambda_n a J_0^2(\lambda_n)}\frac{i\upsilon_n}{\sinh(i\upsilon_n L)}\cosh(i\upsilon_n z)+\frac{I_0}{\lambda_n a J_0^2(\lambda_n)}(i\upsilon_n)\sinh(i\upsilon_n z)\right]J_1\left(\frac{\lambda_n}{a}r\right) \\ &= -\sum_{n=0}^{\infty}\left[\frac{I_L-\cos(\upsilon_n L)I_0}{\lambda_n a J_0^2(\lambda_n)}\frac{i\upsilon_n}{i\sin(\upsilon_n L)}\cos(\upsilon_n z)+\frac{I_0}{\lambda_n a J_0^2(\lambda_n)}(i\upsilon_n)i\sin(\upsilon_n z)\right]J_1\left(\frac{\lambda_n}{a}r\right) \end{aligned} \tag{29}$$

The outcome is of course identical to the type I representation.

Given that λ_n can vary from 3.8317 up to infinity while C remains fixed, $C^2-\lambda_n^2/a^2$ can be either positive or negative. Using k to denote the largest Bessel root to satisfy $\lambda_k \le aC$, we identify two subsets that exhibit the following properties

$$\begin{cases} \upsilon_n^2 = C^2-\lambda_n^2/a^2 \ge 0; \quad \lambda_n \le aC; \quad n=0,\ldots,k \\ (\upsilon_n^*)^2 = \lambda_n^2/a^2 - C^2 > 0; \quad \lambda_n > aC; \quad n=k+1,\ldots,\infty \end{cases} \tag{30}$$

In each of these subsets, υ_n and υ_n^* remain essentially positive real numbers. Then owing to the identity of the type I and type II expressions, we can develop one consolidated formulation with no imaginary parts. This is accomplished by taking

$$\begin{aligned} \psi(r,z) = &\sum_{n=0}^{k} r\left[\frac{I_L-\cos(\upsilon_n L)I_0}{\lambda_n a J_0^2(\lambda_n)\sin(\upsilon_n L)}\sin(\upsilon_n z)+\frac{I_0}{\lambda_n a J_0^2(\lambda_n)}\cos(\upsilon_n z)\right]J_1\left(\frac{\lambda_n}{a}r\right) \\ &+\sum_{n=k+1}^{\infty} r\left[\frac{I_L-\cosh(\upsilon_n^* L)I_0}{\lambda_n a J_0^2(\lambda_n)\sinh(\upsilon_n^* L)}\sinh(\upsilon_n^* z)+\frac{I_0}{\lambda_n a J_0^2(\lambda_n)}\cosh(\upsilon_n^* z)\right]J_1\left(\frac{\lambda_n}{a}r\right) \end{aligned} \tag{31}$$

Similarly, u_z, u_r and u_θ can be expressed as:

$$u_z = \left\{\begin{aligned} &\sum_{n=0}^{k}\left[\frac{I_L-\cos(\upsilon_n L)I_0}{\lambda_n a J_0^2(\lambda_n)\sin(\upsilon_n L)}\sin(\upsilon_n z)+\frac{I_0}{\lambda_n a J_0^2(\lambda_n)}\cos(\upsilon_n z)\right]J_0\left(\frac{\lambda_n}{a}r\right) \\ &+\sum_{n=k+1}^{\infty}\left[\frac{I_L-\cosh(\upsilon_n^* L)I_0}{\lambda_n a J_0^2(\lambda_n)\sinh(\upsilon_n^* L)}\sinh(\upsilon_n^* z)+\frac{I_0}{\lambda_n a J_0^2(\lambda_n)}\cosh(\upsilon_n^* z)\right]J_0\left(\frac{\lambda_n}{a}r\right) \end{aligned}\right\} \tag{32}$$

$$u_r = \left\{\begin{aligned} &-\sum_{n=0}^{k}\left[\frac{I_L-\cos(\upsilon_n L)I_0}{\lambda_n a J_0^2(\lambda_n)\sin(\upsilon_n L)}\upsilon_n\cos(\upsilon_n z)-\frac{I_0}{\lambda_n a J_0^2(\lambda_n)}\upsilon_n\sin(\upsilon_n z)\right]J_1\left(\frac{\lambda_n}{a}r\right) \\ &-\sum_{n=k+1}^{\infty}\left[\frac{I_L-\cosh(\upsilon_n^* L)I_0}{\lambda_n a J_0^2(\lambda_n)\sinh(\upsilon_n^* L)}\upsilon_n^*\cosh(\upsilon_n^* z)+\frac{I_0}{\lambda_n a J_0^2(\lambda_n)}\upsilon_n^*\sinh(\upsilon_n^* z)\right]J_1\left(\frac{\lambda_n}{a}r\right) \end{aligned}\right\} \tag{33}$$

and

$$u_\theta = \left(C^2\left\{\begin{aligned} &\sum_{n=0}^{k}\left[\frac{I_L-\cos(\upsilon_n L)I_0}{\lambda_n a J_0^2(\lambda_n)\sin(\upsilon_n L)}\sin(\upsilon_n z)+\frac{I_0}{\lambda_n a J_0^2(\lambda_n)}\cos(\upsilon_n z)\right]J_1\left(\frac{\lambda_n}{a}r\right) \\ &+\sum_{n=k+1}^{\infty}\left[\frac{I_L-\cosh(\upsilon_n^* L)I_0}{\lambda_n a J_0^2(\lambda_n)\sinh(\upsilon_n^* L)}\sinh(\upsilon_n^* z)+\frac{I_0}{\lambda_n a J_0^2(\lambda_n)}\cosh(\upsilon_n^* z)\right]J_1\left(\frac{\lambda_n}{a}r\right) \end{aligned}\right\}^2+\frac{B_1}{r^2}\right)^{\frac{1}{2}} \tag{34}$$

Equations (32), (33) and (34) constitute the apex of this study and are, therefore, marked as such. To employ this formulation, the arbitrary axial profiles $U_L(r)$ and $U_0(r)$ may be defined based on realistic flow conditions. The specification of u_z at the endwalls leads to the full determination of the source integrals (I_0, I_l). These affect the expression for u_θ. Nonetheless, two additional parameters are still available to control u_θ to the extent of mimicking a given tangential velocity at entry. The tangential velocity is hence prescribed as one can alter u_θ at the endwall by specifying the constants C and B_1 in a manner to match a given injection function. For example, when $B_1 = 0$, a special family of Trkalian flows may be engendered in which no slippage is permitted at the sidewall. Conversely, when $B_1 \ne 0$, an essential singularity ascribed to swirl-dominated inviscid flows appears at the centerline. Once C, I_0 and I_l are determined, both u_z and u_r become available throughout the entire domain. Evidently, any velocity pattern imposed at $z=(0,L)$ must satisfy volume conservation viz.

$$\int_0^a 2\pi r\left[u_z(r,L)-u_z(r,0)\right]\mathrm{d}r = 0 \tag{35}$$

C. Normalization

Using standard reference values, we define

$$\bar{r}=\frac{r}{a},\ \bar{z}=\frac{z}{a},\ \bar{u}_r=\frac{u_r}{U},\ \bar{u}_z=\frac{u_z}{U},\ \bar{u}_\theta=\frac{u_\theta}{U},\ \bar{\psi}=\frac{\psi}{Ua^2},\ \bar{Q}_i=\frac{Q_i}{Ua^2},\ \bar{B}_1=\frac{B_1}{U^2a^2},\ \bar{C}=Ca \tag{36}$$

Implementing the above normalization into our equations, the streamfunction and velocity expressions become

$$\bar{\psi}(\bar{r},\bar{z})=\sum_{n=0}^{k}\bar{r}\left[\frac{\bar{I}_L-\cos(\bar{\upsilon}_n l)\bar{I}_0}{\lambda_n J_0^2(\lambda_n)\sin(\bar{\upsilon}_n l)}\sin(\bar{\upsilon}_n\bar{z})+\frac{\bar{I}_0}{\lambda_n J_0^2(\lambda_n)}\cos(\bar{\upsilon}_n\bar{z})\right]J_1(\lambda_n\bar{r})$$
$$+\sum_{n=k+1}^{\infty}r\left[\frac{\bar{I}_L-\cosh(\bar{\upsilon}_n^* l)\bar{I}_0}{\lambda_n J_0^2(\lambda_n)\sinh(\bar{\upsilon}_n^* l)}\sinh(\bar{\upsilon}_n^*\bar{z})+\frac{\bar{I}_0}{\lambda_n J_0^2(\lambda_n)}\cosh(\bar{\upsilon}_n^*\bar{z})\right]J_1(\lambda_n\bar{r}) \tag{37}$$

$$\bar{u}_z(\bar{r},\bar{z})=\sum_{n=0}^{k}\left[\frac{\bar{I}_l-\cos(\bar{\upsilon}_n l)\bar{I}_0}{\lambda_n J_0^2(\lambda_n)\sin(\bar{\upsilon}_n l)}\sin(\bar{\upsilon}_n\bar{z})+\frac{\bar{I}_0}{\lambda_n J_0^2(\lambda_n)}\cos(\bar{\upsilon}_n\bar{z})\right]J_0(\lambda_n\bar{r})$$
$$+\sum_{n=k+1}^{\infty}\left[\frac{\bar{I}_l-\cosh(\bar{\upsilon}_n^* l)\bar{I}_0}{\lambda_n J_0^2(\lambda_n)\sinh(\bar{\upsilon}_n^* l)}\sinh(\bar{\upsilon}_n^*\bar{z})+\frac{\bar{I}_0}{\lambda_n J_0^2(\lambda_n)}\cosh(\bar{\upsilon}_n^*\bar{z})\right]J_0(\lambda_n\bar{r}) \tag{38}$$

$$\bar{u}_r(\bar{r},\bar{z})=-\sum_{n=0}^{k}\left[\frac{\bar{I}_l-\cos(\bar{\upsilon}_n l)\bar{I}_0}{\lambda_n J_0^2(\lambda_n)\sin(\bar{\upsilon}_n l)}\bar{\upsilon}_n\cos(\bar{\upsilon}_n\bar{z})-\frac{\bar{I}_0}{\lambda_n J_0^2(\lambda_n)}\bar{\upsilon}_n\sin(\bar{\upsilon}_n\bar{z})\right]J_1(\lambda_n\bar{r})$$
$$-\sum_{n=k+1}^{\infty}\left[\frac{\bar{I}_l-\cosh(\bar{\upsilon}_n^* l)\bar{I}_0}{\lambda_n J_0^2(\lambda_n)\sinh(\bar{\upsilon}_n^* l)}\bar{\upsilon}_n^*\cosh(\bar{\upsilon}_n\bar{z})+\frac{\bar{I}_0}{\lambda_n J_0^2(\lambda_n)}\bar{\upsilon}_n^*\sinh(\bar{\upsilon}_n^*\bar{z})\right]J_1(\lambda_n\bar{r}) \tag{39}$$

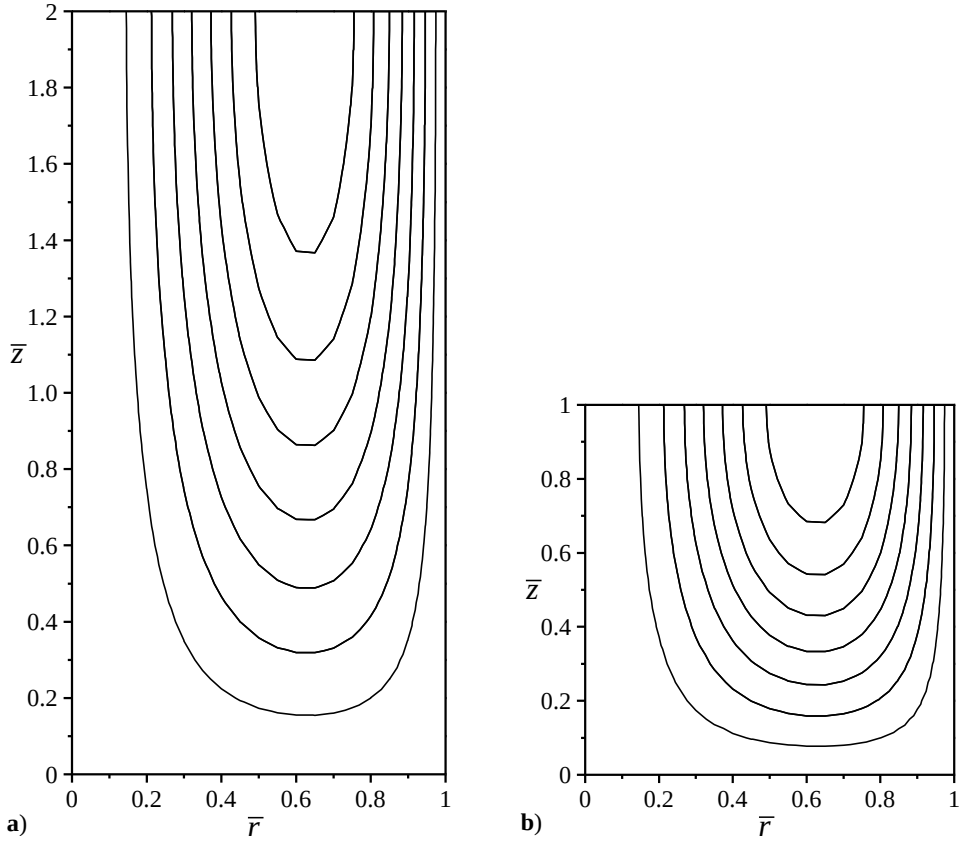

Figure 2. Streamlines for a) *l* = 2 and b) *l* = 1 using the linear Beltramian model at the endwall.

and, for the tangential component,

$$\bar{u}_\theta(\bar{r},\bar{z}) = \left(\bar{C}^2 \left\{ \sum_{n=0}^{k} \left[\frac{\bar{I}_l - \cos(\bar{\upsilon}_n l)\bar{I}_0}{\lambda_n a J_0^2(\lambda_n)\sin(\bar{\upsilon}_n l)} \sin(\bar{\upsilon}_n \bar{z}) + \frac{\bar{I}_0}{\lambda_n a J_0^2(\lambda_n)} \cos(\bar{\upsilon}_n \bar{z}) \right] J_1(\lambda_n \bar{r}) \right.$$

$$\left. + \sum_{n=k+1}^{\infty} \left[\frac{\bar{I}_l - \cosh(\bar{\upsilon}_n^* l)\bar{I}_0}{\lambda_n J_0^2(\lambda_n)\sinh(\bar{\upsilon}_n^* l)} \sinh(\bar{\upsilon}_n^* \bar{z}) + \frac{\bar{I}_0}{\lambda_n J_0^2(\lambda_n)} \cosh(\bar{\upsilon}_n^* \bar{z}) \right] J_1(\lambda_n \bar{r}) \right\}^2 + \frac{\bar{B}_1}{\bar{r}^2} \Bigg)^{\frac{1}{2}} \tag{40}$$

Here the normalized source integrals may be computed from

$$\begin{cases} \bar{I}_l \equiv 2\int_0^1 \bar{u}_z(\bar{r},l)\bar{r}J_0(\lambda_n \bar{r})\,\mathrm{d}\bar{r} & \text{(endwall)} \\ \bar{I}_0 \equiv 2\int_0^1 \bar{u}_z(\bar{r},0)\bar{r}J_0(\lambda_n \bar{r})\,\mathrm{d}\bar{r} & \text{(headwall)} \end{cases} \tag{41}$$

where $\bar{\upsilon}_n^2 = \bar{C}^2 - \lambda_n^2$ and $(\bar{\upsilon}_n^*)^2 = \lambda_n^2 - \bar{C}^2$. It may be instructive to note that the foregoing solution can accommodate arbitrary headwall and endwall velocity patterns, $\bar{u}_z(\bar{r},0)$ and $\bar{u}_z(\bar{r},l)$, so long as the imposed profiles remain observant of the mass conservation principle. Otherwise, the solution initiated with an incongruent model will actually self-correct to the extent of producing a distribution which, when evaluated at the endwalls, will generate a velocity profile that is different from the one originally imposed. The altered profile at the boundary will strongly resemble the one prescribed as an input except for some minor differences that cause it to gracefully satisfy mass conservation. Conversely, when a physical solution that observes continuity is imposed at the endwalls, the resulting series summation will return the same profile as the source. Such self-correcting behavior is quite interesting to note in the present model. It may be ascribed to the series solution being analytic, continuous and infinitely differentiable, in addition to being consistent with mass conservation throughout the entire chamber. These properties instill in our solution an aversion toward sudden unphysical jumps, especially at its boundaries.

III. Results and Discussion

A. Flow Streamlines

From Eq. (37), one can reproduce the streamlines shown in Fig. 2 for aspect ratios of $l = 2$ and $l = 1$. Our flow is symmetrical about the chamber axis, and so it is sufficient to plot fluid trajectories in two dimensions over $0 \le \bar{r} \le 1$ and $0 \le \bar{z} \le l$. The patterns displayed in both plots seem to be in fair agreement with the experimental data on gas cyclones acquired by Smith[17,18] and with the numerical results reported by Fang, Majdalani and Chiaverini.[19,20]

In generating these streamlines, the profile corresponding to the axial velocity used by Majdalani,[16] $\bar{u}_z(\bar{r},l) = 11.76\kappa l J_0(\lambda_0 \bar{r})$, is imposed at the endwall. The tangential inflow parameter κ is introduced for the sake of consistency in the comparison with Majdalani's solution. As usual, we take $\kappa = (2\pi\sigma l)^{-1}$ where $\sigma = a^2 / A_i$ is the swirl number. For a rigid headwall with no injection, the second boundary condition is set as $\bar{u}_z(\bar{r},0) = 0$.

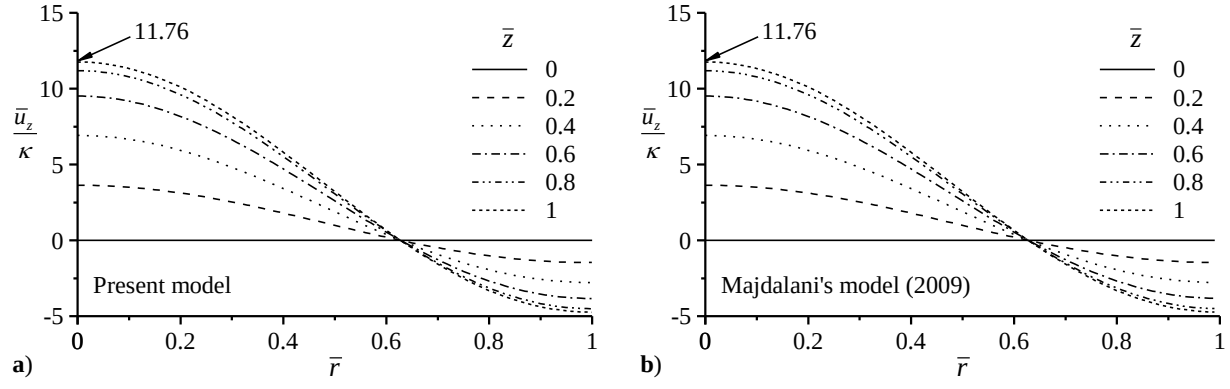

Figure 3. Comparison between the axial velocities corresponding to a) Eq. (38) and b) the linear Beltramian formulation by Majdalani.[16] Here *l* = 1.

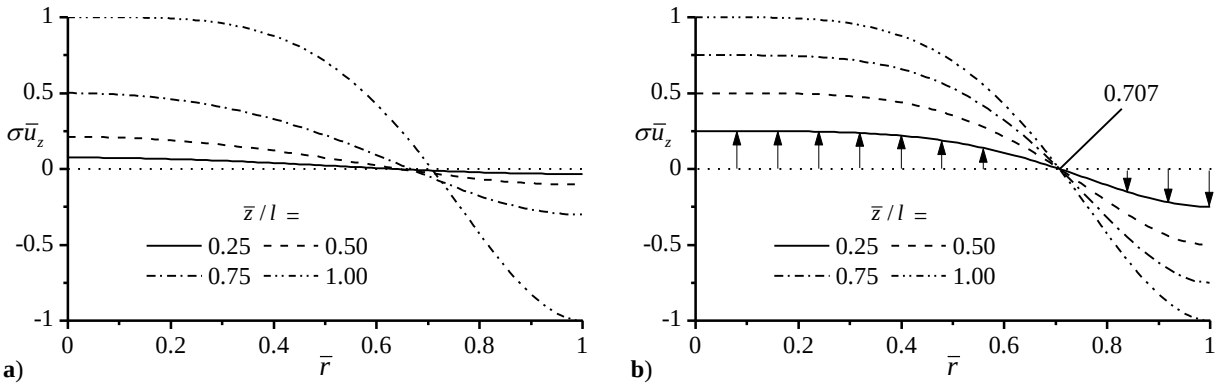

Figure 4. Comparison between the axial velocities corresponding to a) Eq. (38) and b) the complex-lamellar solution.[24]

Table 1. Mantle location obtained using the complex-lamellar endwall profile[24]

Location	$\bar{z}/l$	$\bar{r}$
1	0.25	0.637
2	0.5	0.645
3	0.75	0.665
4	1	0.707
Mean		**0.6635**

B. Axial Velocity

Figure 3a displays our axial profiles using the endwall velocity at $\bar{z} = l$ that is defined in the previous section. Directly to the right, Fig. 3b presents the Beltramian axial velocity profile obtained by Majdalani.[16] Although the two analytical studies use different approaches, it may be seen that their solutions generate identical profiles for $\sigma\bar{u}_z$. The striking resemblance in the two results is mainly due to the two analyses using analogous approximations and assumptions including the BHE approach as their point of departure. Furthermore, the eigenvalue λ_0 used by Majdalani[16] belongs to the subset of eigenvalues appended into the generalized framework developed here.

Given the dual polarity of the axial velocity in these graphs, the mantle location may be identified at the point where $\bar{u}_z$ vanishes. The corresponding point on the mantle is found to be fixed at $\bar{r} = 0.6276$. This result is reassuring in view of the numerical work by Hoekstra, Derksen and van den Akker[25] who also report the location of zero axial velocity to be close to $\bar{r} \approx 0.675$. Also found in the literature are some experimental results by Smith[17,18] for gas cyclones that fall near a mean mantle location of $\bar{r} \approx 0.6166$. In comparing these various findings, the disparity in mantle prediction seems to range between 1.8 and 7 percent. The small discrepancy with respect to our prediction may be attributed to the linear approximation in Eq. (6) and the inviscid assumptions adopted here. In fact, the numerical and experimental studies conducted so far all display slight geometric differences that can have an added bearing on the mantle location. Examples include Smith[17,18] who compiled two sets of laboratory measurements and these showed the mantle at either 0.617 or 0.721. His experiments exhibited dissimilarities in the injection Reynolds number and protrusion depth of the vortex finder. Along similar lines, we note that the location of the mantle does not remain fixed in the present model but rather depends on the input profile. What triggers such spatial sensitivity will be expounded below.

To further visualize the behavior of Eq. (23), we present $\bar{u}_z$ in Fig. 4 and compare it to the complex-lamellar counterpart due to Vyas and Majdalani.[24] It can be seen that the increase in axial velocity at the center and the decrease at the sidewall are both linear in Fig. 4b. In contrast, the acceleration displayed in Fig. 4a is no longer constant. The variation in the axial velocities rather follows a slightly nonlinear behavior that appears to be consistent with the experimental measurements reported by Smith.[17,18]

Returning to Fig. 4b, a constant position of the mantle may be seen at $\bar{r} = 0.707$ irrespective of the axial position. Conversely, in Fig. 4a this location is seen to slightly vary. The spatial variability of the mantle is captured in Table 1 where points belonging to the mantle surface are calculated from the analytical solution at

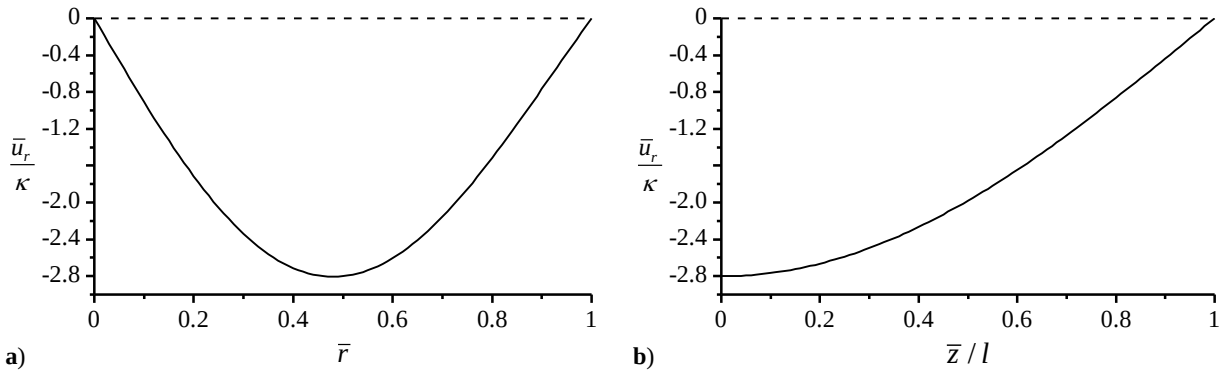

Figure 5. Radial velocities corresponding to Eq. (39) shown in both a) radial ($\bar{z}$ = 0) and b) axial ($\bar{r}$ = 0.48) directions.

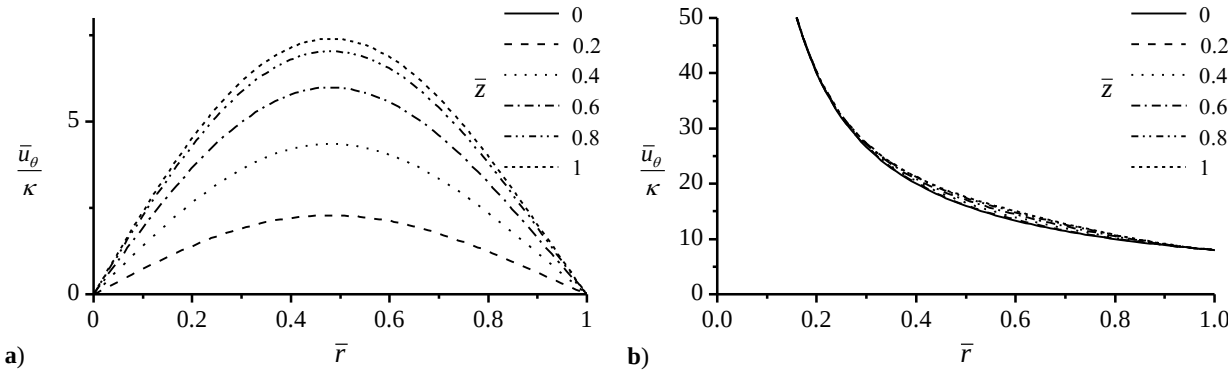

Figure 6. Behavior of the tangential velocity shown at different axial positions for a) Trkalian and b) Beltramian input conditions. Here *l* = 1 and κ = 0.125.

various heights. Note that the mantle position at $\bar{z} = l$, namely 0.707, is determined according to the axial velocity profile imposed at the endwall. In matching the endwall pattern, the mantle does not maintain a fixed location. The variability displayed by the analytical model is similar to the physical behavior reported in the experiments by Smith.[17,18] Therein, the mantle is shown to vary in one case from $\bar{r} = 0.583$ to 0.663 while traversing 10.7 inches of chamber length, and in the other, from $\bar{r} = 0.708$ to 0.721 while using a different vortex finder and Reynolds number. The difference between the latter and the values posted in Table 1 may be due to a variety of reasons. These include the inviscid assumption imposed in our formulation and the bias caused by the internal protrusion of the vortex finder, a standard component of gaseous cyclones.

C. Radial Velocity

The radial velocity vanishes at the centerline due to axial symmetry. Unlike solid or hybrid rocket motors, the vortex-fired rocket engines do not exhibit any radial velocity at the sidewall. This can be clearly seen in Fig. 5a. The maximum radial velocity is shown to occur around $\bar{r}_{\max} = 0.48$, a position that fully agrees with the value reported by Majdalani.[16]

Figure 5b follows the variation of the radial velocity at $\bar{r} = 0.48$ in the axial direction. Although we do not enforce the condition $\bar{u}_r = 0$ at the endwall, it can be seen nonetheless that $\bar{u}_r$ vanishes at $\bar{z} = l$ and increases in magnitude to reach its maximum at the headwall. In general, the magnitude of the radial velocity remains small compared to its axial companion except in the region near the headwall where the radial velocity peaks at the same time as its axial counterpart gradually vanishes.

D. Tangential Velocity

The tangential velocity at $\bar{z} = l$ is dependent on the choice of $\bar{u}_z(\bar{r}, l)$. The two constants C and $\bar{B}_1$ grant us two degrees of freedom by providing two parameters that can be adjusted to the extent of accounting for different tangential velocity profiles at the endwalls. To demonstrate the flexibility of our solution, we consider the axial

profiles by Majdalani[16] for which two distinct cases may be chosen, each featuring a different tangential velocity at the inlet.

Figure 6a is based on Eq. (40) using Majdalani's slip-resistant Trkalian profile in the axial direction.[16] In this case, we set $\bar{B}_1 = 0$ in the tangential velocity expression in order to ensure that it vanishes at $\bar{r} = 0$. We then adjust the parameter $\bar{C}$ to match the magnitude of the velocity at the endwall. Because the inlet tangential speed observes the no-slip requirement at the sidewall, the velocity-adherence property is carried through the rest of the domain. For example, it can be seen that $\bar{u}_\theta$ at $\bar{r} = 1$ vanishes along the length of the chamber. Evidently such will not be the behavior under different inlet conditions, especially when using motions that permit slip at the sidewall.

Our second test case provides an illustration of the latter situation. Now we use the linearly varying Beltramian profile with a slip permitting tangential velocity at $\bar{z} = l$.[16] The corresponding $\bar{u}_\theta(\bar{r}, l)$ displays a hyperbolic relation with the radial distance, thus causing $\bar{u}_\theta$ to approach a nonzero value at the sidewall and infinity at the centerline. In our effort at matching this free-vortex motion, both $\bar{C}$ and $\bar{B}_1$ are carefully selected. The resulting solution in Fig. 6b displays minute excursions in the tangential velocity at different axial positions. Such behavior is identical to the one reported by Majdalani.[16]

IV. Conclusions

This study presents an exact Euler solution for the swirling flow in a bidirectional vortex chamber. What distinguishes this new set of analytical results is the model's capability to absorb arbitrary flow conditions at the endwall boundaries. Due to the lack of experimental data from which well-defined profiles may be extrapolated, we have mainly resorted to comparisons with former analytical solutions.

As it may be anticipated, our axial velocity displays the tendency to reproduce the same profiles imposed at the endwalls although its shapes may often shift in the axial direction as the flow changes from its basic configuration to the one prescribed at its boundary. In all of the cases tested, the magnitude of the axial speed is seen to decrease in a nonlinear way until it vanishes at the headwall. This behavior seems somewhat consistent with the measurements obtained in two experiments by Smith.[17,18]

Although we do not impose the radial velocity at the boundary, we are able to extract the same results as Majdalani[16] who forces his radial velocity, $\bar{u}_r$, to vanish along the entire endwall. By setting in our model the inviscid Beltramian $\bar{u}_z$ as an inlet condition, we realize that we indirectly impose the same radial velocity used in the preceding study. This outcome may be attributed to $\bar{u}_z$ and $\bar{u}_r$ being intimately linked through the axisymmetric continuity relation, and this connection remains independent of the tangential velocity. So by imposing $\bar{u}_z$ at the boundary, we are implicitly securing its unique companion $\bar{u}_r$ at the same location. Regarding size considerations, the magnitude of $\bar{u}_r$ appears to be small in comparison to the axial and tangential speeds. It peaks as we approach the headwall where a larger radial velocity is needed to assist the fluid in crossing from the outer vortex into the central core region (see also Fig. 1b).

Concerning the swirl velocity, two keystone parameters, $\bar{C}$ and $\bar{B}_1$, are calibrated to match the tangential velocity at the boundary. We find that the choice of $\bar{C}$, and therefore $\bar{u}_\theta$ at the endwall, can affect the variation of the axial velocities throughout the domain. Using Eq. (40), we are able to reproduce both Trkalian and Beltramian motions described in previous work by Majdalani.[16]

Acknowledgments

This project was completed with support from the National Science Foundation through Grant No. CMMI-0928762, Dr. Eduardo A. Misawa, Program Director.

References

[1]Gloyer, P. W., Knuth, W. H., and Goodman, J., "Overview of Initial Research into the Effects of Strong Vortex Flow on Hybrid Rocket Combustion and Performance," CSTAR Fifth Annual Symposium Paper N96-16953, January 1993.

[2]Knuth, W. H., Bemowski, P. A., Gramer, D. J., Majdalani, J., and Rothbauer, W. J., "Gas-Fed, Vortex Injection Hybrid Rocket Engine," NASA Marshall Space Flight Center, SBIR Phase I Final Technical Rept. NASA/MSFC Contract NAS8-40679, Huntsville, AL, August 1996.

[3]Chiaverini, M. J., Malecki, M. J., Sauer, J. A., Knuth, W. H., and Majdalani, J., "Vortex Thrust Chamber Testing and Analysis for O2-H2 Propulsion Applications," AIAA Paper 2003-4473, July 2003.

[4]Matveev, I., Matveeva, S., and Serbin, S., "Design and Preliminary Test Results of the Plasma Assisted Tornado Combustor," AIAA Paper 2007-5628, July 2007.

[5]Vyas, A. B., Majdalani, J., and Chiaverini, M. J., "The Bidirectional Vortex. Part 1: An Exact Inviscid Solution," AIAA Paper 2003-5052, July 2003.

[6]Vyas, A. B., Majdalani, J., and Chiaverini, M. J., "The Bidirectional Vortex. Part 2: Viscous Core Corrections," AIAA Paper 2003-5053, July 2003.

[7]Vyas, A. B., Majdalani, J., and Chiaverini, M. J., "The Bidirectional Vortex. Part 3: Multiple Solutions," AIAA Paper 2003-5054, July 2003.

[8]Majdalani, J., and Vyas, A. B., "Rotational Axisymmetric Mean Flow for the Vortex Injection Hybrid Rocket Engine," AIAA Paper 2004-3475, July 2004.

[9]Majdalani, J., "Vortex Injection Hybrid Rockets," *Fundamentals of Hybrid Rocket Combustion and Propulsion*, edited by K. Kuo and M. J. Chiaverini, AIAA Progress in Astronautics and Aeronautics, Washington, DC, 2007, pp. 247-276.

[10]Vyas, A. B., and Majdalani, J., "Characterization of the Tangential Boundary Layers in the Bidirectional Vortex Thrust Chamber," AIAA Paper 2006-4888, July 2006.

[11]Batterson, J. W., and Majdalani, J., "On the Boundary Layers of the Bidirectional Vortex," AIAA Paper 2007-4123 June 2007.

[12]Batterson, J. W., and Majdalani, J., "Sidewall Boundary Layers of the Bidirectional Vortex," *Journal of Propulsion and Power*, Vol. 26, No. 1, 2010, pp. 102-112. doi: 10.2514/1.40442

[13]Majdalani, J., and Chiaverini, M. J., "On Steady Rotational Cyclonic Flows: The Viscous Bidirectional Vortex," *Physics of Fluids*, Vol. 21, No. 10, 2009, pp. 10360301-15. doi: 10.1063/1.3247186

[14]Maicke, B. A., and Majdalani, J., "A Constant Shear Stress Core Flow Model of the Bidirectional Vortex," *Proceedings of the Royal Society of London, Series A*, Vol. 465, No. 2103, 2009, pp. 915-935. doi: 10.1098/rspa.2008.0342

[15]Zhao, J. Q., and Abrahamson, J., "The Flow in Cylindrical Cyclones," *Developments in Chemical Engineering and Mineral Processing*, Vol. 11, No. 3-4, 2003, pp. 201-222. doi: 10.1002/apj.5500110403

[16]Majdalani, J., "Exact Eulerian Solutions of the Cylindrical Bidirectional Vortex," AIAA Paper 2009-5307, August 2009.

[17]Smith, J. L., "An Experimental Study of the Vortex in the Cyclone Separator," *Journal of Basic Engineering-Transactions of the ASME*, Vol. 84, No. 4, 1962, pp. 602-608.

[18]Smith, J. L., "An Analysis of the Vortex Flow in the Cyclone Separator," *Journal of Basic Engineering-Transactions of the ASME*, Vol. 84, No. 4, 1962, pp. 609-618.

[19]Fang, D., Majdalani, J., and Chiaverini, M. J., "Simulation of the Cold-Wall Swirl Driven Combustion Chamber," AIAA Paper 2003-5055, July 2003.

[20]Fang, D., Majdalani, J., and Chiaverini, M. J., "Hot Flow Model of the Vortex Cold Wall Liquid Rocket," AIAA Paper 2004-3676, July 2004.

[21]Rom, C. J., "Flow Field and near Nozzle Fuel Spray Characterizations for a Cold Flowing Vortex Engine," M.S. Dissertation, University of Wisconsin, 2006.

[22]Rom, C. J., Anderson, M. H., and Chiaverini, M. J., "Cold Flow Analysis of a Vortex Chamber Engine for Gelled Propellant Combustor Applications," AIAA Paper 2004-3359, July 2004.

[23]Hu, L. Y., Zhou, L. X., Zhang, J., and Shi, M. X., "Studies of Strongly Swirling Flows in the Full Space of a Volute Cyclone Separator," *AIChE Journal*, Vol. 51, No. 3, 2005, pp. 740-749. doi: 10.1002/aic.10354

[24]Vyas, A. B., and Majdalani, J., "Exact Solution of the Bidirectional Vortex," *AIAA Journal*, Vol. 44, No. 10, 2006, pp. 2208-2216. doi: 10.2514/1.14872

[25]Hoekstra, A. J., Derksen, J. J., and Van den Akker, H. E. A., "An Experimental and Numerical Study of Turbulent Swirling Flow in Gas Cyclones," *Chemical Engineering Science*, Vol. 54, No. 13, 1999, pp. 2055-2065. doi: 10.1016/S0009-2509(98)00373-X